

Indicator Cokriging-Based Subpixel Land Cover Mapping With Shifted Images

Qunming Wang, Wenzhong Shi, and Liguang Wang

Abstract—Subpixel mapping (SPM) is a technique for predicting the spatial distribution of land cover classes in remote sensing images at a finer spatial resolution level than those of the input images. Indicator cokriging (ICK) has been found to be an effective and efficient SPM method. The accuracy of this model, however, is limited by insufficient constraints. In this paper, the accuracy of the ICK-based SPM model is enhanced by using additional information gained from multiple shifted images (MSIs). First, each shifted image is utilized to compute the conditional probability of class occurrence at any fine spatial resolution pixel (i.e., subpixel) using ICK, and a set of conditional probability maps for all classes are generated for each image. The multiple ICK-derived conditional probability maps are then integrated, according to the estimated subpixel shifts of MSI. Lastly, class allocation at the subpixel scale is implemented to produce SPM results. The proposed algorithm was tested on two synthetic coarse spatial resolution remote sensing images and a set of real Moderate Resolution Imaging Spectroradiometer (MODIS) data. It was evaluated both visually and quantitatively. The experimental results showed that more accurate SPM results can be generated with MSI than with a single observed coarse image in conventional ICK-based SPM. In addition, the accuracy of the proposed method is higher than that of the existing Hopfield neural network (HNN)-based SPM and the HNN with MSI.

Index Terms—Indicator cokriging (ICK), indicator semivariogram, land cover, shifted images, super-resolution mapping.

I. INTRODUCTION

MAN has extended his view of the land to space by using remote sensing images, hence greatly improving the observation depth of the earth. Land cover classification is an important technique to extract land cover information from remote sensing images. It has been a key issue in remote sensing for many years. Conventional classification techniques allocate each pixel to a single land cover class. This type of technique is

known as hard classification. It is not sufficient for hard classification to provide the detailed information concerning the spatial distribution of land cover classes, as mixed pixels exist widely in remote sensing images. A mixed pixel contains more than one class. References [1] and [2] illustrate some common origins of mixed pixel problems. Whatever the spatial resolution of the sensor, mixed pixels are unavoidable in remote sensing images and usually the aim of investigators is to extract information that is smaller than pixel size [1].

The soft classification has been developed to extract land cover information from remote sensing images in an attempt to solve mixed pixel problems. Commonly used instances include linear spectral mixture analysis [3], fuzzy *c*-means classifiers [4], artificial neural networks [5], *k*-nearest neighbor classifiers [6], support vector machines [7], [8], and nonlinear unmixing [9]. The outputs of soft classification, however, are fractions of the classes within the mixed pixels. Soft classification fails to predict the spatial locations of the classes. The subpixel mapping (SPM, also termed *super-resolution mapping* in the remote sensing literature) [10] is a technique to address this problem, by dividing each mixed pixel into multiple subpixels and predicting their class values. The number of subpixels belonging to each class depends on the outputs of soft classification. SPM results in an increase in spatial resolution above the conventional hard classification of the input remote sensing images. In nature, SPM transforms the soft classification into a finer scaled hard classification.

After Atkinson mentioned that SPM can be considered as the postprocessing of soft classification based on the spatial dependence theory [10], many SPM algorithms have been continuously developed. Verhoeve and De Wulf [11] proposed a spatial dependence mathematical model and adopted linear optimization techniques to maximize the dependence. Considering each subpixel as a neuron, [12]–[14] set up an energy function for a Hopfield neural network (HNN). This function increases the spatial correlation between neighboring subpixels, taking account of class constraints. The energy function is minimized iteratively to generate SPM results. Mertens *et al.* [15] constructed a goal function evaluating the sum of the neighboring values of all subpixels and used a genetic algorithm to search for the most possible configuration. According to the defined attractiveness in [16], a pixel swapping algorithm was introduced that exchanged two subpixel classes most in need of swapping within coarse pixel and SPM results were approached iteratively. Mertens *et al.* [17] applied subpixel/pixel spatial attraction models to calculate the spatial attractions between subpixels and their neighboring pixels. Ge *et al.* [18] utilized the fractions in the neighboring coarse pixels to draw a linear boundary for each class inside each centre coarse pixel. Wang

Manuscript received December 20, 2012; revised February 23, 2013; accepted April 11, 2013. Date of publication May 23, 2013; date of current version December 18, 2013. This work was supported in part by Ministry of Science and Technology of China under Grant 2012BAJ15B04 and in part by the National Natural Science Foundation of China under Grant 61275010. (Corresponding author: W. Shi.)

Q. Wang is with the Department of Land Surveying and Geo-Informatics, The Hong Kong Polytechnic University, Kowloon, Hong Kong (e-mail: wqm11111@126.com).

W. Shi is with the Joint Research Laboratory on Spatial Information, The Hong Kong Polytechnic University, Hong Kong, and Wuhan University, Wuhan 430072, China (e-mail: lswzshi@polyu.edu.hk).

L. Wang is with the College of Information and Communications Engineering, Harbin Engineering University, Harbin 150001, China (e-mail: wangliguo@hrbeu.edu.cn).

Color versions of one or more of the figures in this paper are available online at <http://ieeexplore.ieee.org>.

Digital Object Identifier 10.1109/JSTARS.2013.2262927

et al. [19] studied the essence of the pixel swapping algorithm and introduced the particle swarm optimization to maximize the correlation between subpixels after the application of the subpixel/pixel spatial attraction models-based SPM process. In [20], spatial attractions both between and within pixels were considered simultaneously for SPM. In addition, the Markov random field (MRF)-based SPM method considers spatial and spectral constraints simultaneously for SPM [21], [22].

Using the prior spatial structure information from available high spatial resolution images, some learning-based SPM methods were developed, including the back-propagation (BP) neural network, two-point histogram, and indicator cokriging (ICK). The learning-based SPM algorithms are able to decrease the inherent uncertainty in SPM to some extent, especially when the spatial distribution of classes is complex or in the L-resolution case [23]. The results of the learning-based SPM algorithms are, theoretically, expected to be more objective than those of the methods that only make use of spatial dependence, such as HNN, subpixel/pixel spatial attraction models, and pixel swapping algorithm. Specifically, [24]–[28] presented a BP neural network-based SPM approach, which extracts the relationship between fine class labels and coarse fractions from the training image (i.e., a high spatial resolution image). The performance of BP neural network, however, relies on the training sample numbers, and highly accurate SPM results are more likely to be generated with sufficient training data. Actually, acquiring sufficient training data is a challenge in practical application. Furthermore, in the fitting of the model, many parameters need to be determined, such as the number of iterations, the number of hidden layers and nodes for each hidden layer, the learning rate, and the momentum rate. Atkinson [29] introduced a two-point histogram-based method, which optimized the randomly initialized subpixel maps with maintained class fractions by swapping subpixel classes within pixels to gradually match the two-point histogram extracted from the training image. This algorithm involves a number of iterations, and much time is consumed in the optimization. In addition, the random initialization and stochastic processes during the optimization bring uncertainty in the SPM result. Boucher *et al.* proposed an ICK-based SPM model in [30]–[33]. In this model, the prior spatial structure of each class can be utilized by extracting the indicator semivariogram from fine spatial resolution images. This model contains two steps: 1) computing conditional probabilities of class occurrence at fine pixels and 2) allocating classes for these fine pixels. Different from the learning-based BP neural network that requires as much prior spatial structure information as possible to train the network, ICK-based SPM also works well when limited prior information is available. This is well illustrated by [34], which extracted indicator semivariogram from a representative local area (2% of the entire study area) for ICK-based SPM. By using the limited target resolution reference data, ICK-based SPM produced SPM results of comparable accuracy, with those using a globally derived spatial structure.

ICK-based SPM has several characteristics and advantages:

- The additional information of informed fine spatial resolution pixels (i.e., the class labels of these pixels are known from prior information) can be coded easily into the model

by ICK. These fine pixels can be selected randomly and are not necessarily to locate together, as long as these class labels and their locations are available.

- It is free of any iteration process as the conditional probabilities are obtained by solving a system of equations via ICK and the class allocation is a single-pass method. This is quite different from the SPM methods in [12]–[16], [19]–[22] and the learning-based two-point histogram [29], in which the algorithms evolve gradually to convergence to a stable solution. Hence, by using ICK-based SPM, time spent on iterations can be saved, and the uncertainty introduced by random initialization and stochastic processes during the iterations can also be avoided.
- Few parameters are involved in this model. For ICK-based SPM, often a neighborhood window is considered for each coarse pixel for computational efficiency reasons [30]. Many available SPM models have their own parameters, such as the control parameter in the MRF model [22], the nonlinear parameter in the distance dependent weightings in the pixel swapping algorithm [35], [36] and the pseudo temperature [37], and the weightings in the energy function of HNN. Certainly, much extra work would be done to estimate the optimum parameters, and a change in these parameters may lead to uncertainty in SPM results. However, these would not be the cases if the ICK-based SPM method is used.

The SPM problem is underdetermined in that it has multiple plausible solutions, and many fine spatial resolution land cover maps can lead to an equally good reproduction of the input coarse imagery [30]. Although the ICK-based SPM is able to make use of the spatial structure information from fine spatial resolution images and informed fine pixels, it may still be insufficient to deal with the uncertainty in SPM, especially when the zoom scale is large. The accuracy of SPM will certainly be limited by the large uncertainty involved. The additional information from other data can be useful in addressing the underdetermined problem.

In order to produce more detailed and accurate subpixel land cover maps, some SPM techniques have been developed for use of supplementary information. Foody [38] sharpened fraction images with additional finer spatial resolution image of the same scene to provide a more informative representation of the classes within coarse pixels. Aplin and Atkinson [39] introduced a per-field classification-based SPM method by using auxiliary land-line vector boundaries to refine the distribution of classes within each polygon. In [40], the two-point histogram-based SPM model was enhanced by adding proportion constraints obtained from intermediate spatial resolution panchromatic images to the objective function of this model. Nguyen *et al.* [41] applied the elevation data from LIDAR data to add a height function to HNN. Ling *et al.* [42] obtained the terrain of land cover from digital elevation models and modified the waterline mapping results according to such elevations. Aiming at SPM for urban buildings, Ling *et al.* [43] employed an anisotropic model by incorporating the prior shape information and enhancing the spatial dependence in some directions. Based on HNN, [44]–[47] presented some methods to provide additional proportion constraints for the energy function of HNN. In de-

tail, Nguyen *et al.* [44] obtained the fraction of each class at intermediate spatial resolution from panchromatic images. Similarly, Nguyen *et al.* [45] fused panchromatic and multispectral images to obtain a multispectral image at the spatial resolution of the panchromatic image, and soft classification of the fused image were implemented to obtain the fractions at intermediate spatial resolution. References [46] and [47] added soft classification outputs of multiple shifted images (MSI) to HNN.

As observation satellites have multiobservation capability, they can capture images of the same area once every several days. For instance, the revisit interval of QuickBird is one to six days and MODIS covers the Earth on a daily basis [48]. These images are similar to each other, but they are not completely identical. Because of the slight orbit translations and the Earth's rotation, these images are usually shifted at the subpixel level [46], [49]–[51]. MSIs have been widely used for super-resolution image reconstruction in the field of digital image processing, medical imaging, etc. [52]. Super-resolution reconstruction is different from the SPM studied in this paper: continua are predicted in the former, while categories are predicted in the latter. Further details on the differences between the two types of super-resolution algorithms can be found in [46] and [49]. MSIs are also termed time-series images in remote sensing, which have received increasing attention in land cover mapping and monitoring in recent years [53], [54]. Evidently, the accuracy of SPM based on a single date image can be enhanced by borrowing information from images before and after it in time [49].

The shifted observed images in the SPM model are also coarse spatial resolution images that are usually acquired by the same type of sensor. Therefore, the MSIs are easily acquired, and the geometric correction and reflectance retrievals between different spatial resolution images will be avoided. For this reason and the advantages of ICK-based SPM, this paper presents a new SPM method that uses the additional information from MSI to produce more accurate SPM results using ICK. For MSI, the corresponding multiple conditional probability maps are obtained with ICK, and then the ICK-derived probabilities are integrated for each subpixel. The integrated probabilities are finally used to determine the subpixel class labels. Similar to ICK-based SPM, the proposed algorithm is performed based on the existence of prior spatial structure information of land cover that is representative of the studied area. It inherits all the advantages of the ICK-based SPM: it is able to incorporate the information from the informed fine pixels, no parameters except the neighborhood window size are involved, and it is free of iteration.

The rest of this paper is organized as follows. In Section II, the background of ICK-based SPM is briefly described, followed by details of using MSI. Experimental results are provided in Section III and discussed in Section IV, followed by conclusions in Section V.

II. METHODS

A. ICK-Based SPM

The ICK-based SPM model consists of two steps: computing conditional probabilities and allocating classes, which are briefly described below [30]–[33].

Let Y be the observed coarse spatial resolution image with N pixels and X be the subpixel map at the target spatial resolution with M pixels. Here, $M/N = S^2$, where S is the zoom scale factor (i.e., each coarse pixel is divided into S^2 subpixels). Suppose $c(v)$ denotes the class label of a subpixel v and $c(v) = k$, $k = 1, 2, \dots, K$, where K is the total number of classes in the area studied. Define the binary class indicator for the k th class $i_k(v)$ as

$$i_k(v) = \begin{cases} 1, & \text{if } c(v) = k \\ 0, & \text{otherwise.} \end{cases} \quad (1)$$

In the ICK model, the spatial pattern of the k th class at the fine spatial resolution is characterized by the corresponding k th class indicator semivariogram $\gamma_k(\mathbf{h})$, which is defined as

$$\gamma_k(\mathbf{h}) = \frac{1}{2N(\mathbf{h})} \sum_{p=1}^{N(\mathbf{h})} [i_k(v_p) - i_k(v_p + \mathbf{h})]^2 \quad (2)$$

where $N(\mathbf{h})$ is the number of paired pixels at a specific lag \mathbf{h} from the center pixel v_p . The indicator semivariogram for each land cover class is usually obtained from the prior spatial structure.

Let $a_k(V)$ be the k th class fraction in a coarse pixel V . The fine-to-coarse spatial resolution semivariogram between the k th class indicator $i_k(v_m)$ at the fine pixel v_m and the k th class fraction $a_k(V_n)$ at the coarse pixel V_n is calculated as

$$\gamma_k(v_m, V_n) = \frac{1}{S^2} \sum_{m'=1}^{S^2} \gamma_k(\mathbf{h}_{mm'}) \quad (3)$$

where $\mathbf{h}_{mm'}$ denotes the separation vector between the centroid of v_m and the centroid of any fine pixel $v_{m'}$ within V_n . Similarly, the coarse-to-coarse spatial resolution semivariogram between any two coarse pixels V_n and $V_{n'}$ can be calculated as

$$\gamma_k(V_n, V_{n'}) = \frac{1}{S^4} \sum_{m=1}^{S^2} \sum_{m'=1}^{S^2} \gamma_k(\mathbf{h}_{mm'}) \quad (4)$$

where $\mathbf{h}_{mm'}$ denotes the separation vector between the centroid of any fine pixel v_m within V_n and the centroid of any fine pixel $v_{m'}$ within $V_{n'}$.

The semivariogram models in (2)–(4) are used to estimate the conditional probabilities of class occurrence at fine pixels, and ICK is utilized for this purpose. Let all fractions for the k th class be arranged in a $(N \times 1)$ vector $\mathbf{a}_k = [a_k(V_n), n = 1, 2, \dots, N]^T$. Define the k th global class fraction π_k as the mean of all elements in vector \mathbf{a}_k . Suppose there are G informed fine pixels v_g available and the G indicators for the k th class are arranged in a $(G \times 1)$ vector $\mathbf{j}_k = [i_k(v_g), g = 1, 2, \dots, G]^T$. The ICK-derived probability $p_k(v_m)$, which denotes the probability of the k th class occurrence at fine pixel v_m ($m = 1, 2, \dots, M$), can be computed as

$$p_k(v_m) = \boldsymbol{\eta}_k(v_m)^T \mathbf{a}_k + \boldsymbol{\lambda}_k(v_m)^T \mathbf{j}_k + \pi_k [1 - \text{sum}(\boldsymbol{\eta}_k(v_m)^T) - \text{sum}(\boldsymbol{\lambda}_k(v_m)^T)] \quad (5)$$

where $\boldsymbol{\eta}_k(v_m)$ and $\boldsymbol{\lambda}_k(v_m)$ denotes the ICK weights for the k th class, which are $(N \times 1)$ and $(G \times 1)$ vectors of weights for the N coarse pixels and G informed fine pixels, respectively. The

function $\text{sum}(\bullet)$ takes the sums of all the elements in vector \bullet . The weights $\boldsymbol{\eta}_k(v_m)$ and $\boldsymbol{\lambda}_k(v_m)$ are calculated by solving the ICK system of equations

$$\begin{bmatrix} \mathbf{\Gamma}_k^{VV} & \mathbf{\Gamma}_k^{Vv} \\ \mathbf{\Gamma}_k^{vV} & \mathbf{\Gamma}_k^{vv} \end{bmatrix} \begin{bmatrix} \boldsymbol{\eta}_k(v_m) \\ \boldsymbol{\lambda}_k(v_m) \end{bmatrix} = \begin{bmatrix} \boldsymbol{\gamma}_k^{vV}(v_m) \\ \boldsymbol{\gamma}_k^{vv}(v_m) \end{bmatrix} \quad (6)$$

where $\mathbf{\Gamma}_k^{VV}$ is an $(N \times N)$ matrix of coarse-to-coarse spatial resolution semivariogram values between all pairs of coarse pixels [see (4)], $\mathbf{\Gamma}_k^{Vv}$ is a $(G \times N)$ matrix of fine-to-coarse spatial resolution semivariogram values between all pairs of informed fine and coarse pixels [see (3)], $\mathbf{\Gamma}_k^{vv}$ is a $(G \times G)$ matrix of indicator semivariogram values between all pairs of informed fine pixels, and $\mathbf{\Gamma}_k^{vV} = [\mathbf{\Gamma}_k^{Vv}]^T$. The term $\boldsymbol{\gamma}_k^{vV}(v_m)$ denotes a $(N \times 1)$ vector of fine-to-coarse semivariogram values between the uninformed fine pixel v_m and all N coarse pixels, and $\boldsymbol{\gamma}_k^{vv}(v_m)$ denotes a $(G \times 1)$ vector of semivariogram values between v_m and all G informed fine pixels.

The goal of SPM is to generate hard classified maps at subpixel level, and the ICK-derived probabilities are used to decide the subpixel class labels. In the conventional ICK-based SPM, a sequential indicator simulation is employed for class allocation, by which the hard classified map is generated along a random simulation path determining the order of visited subpixels. There is much randomness as there are $S^2!$ paths for each coarse pixel in all. As a result, many speckle artifacts appear in the SPM results [33]. Actually, the class allocation process can also be realized by using a different sequential method that assigns each class in turn [55]. In this approach, a visiting order for all classes is predetermined. According to the visiting order, the subpixels belonging to the visited class are determined by comparing S^2 probabilities for this class and the remaining ones are then used for the allocation of the next class. This approach is also implemented under the condition that the number of subpixels for the k th class within V is constrained to reproduce exactly the corresponding coarse fraction $a_k(V)$ ($k = 1, 2, \dots, K$).

B. Using MSI as Additional Information for ICK-Based SPM

The essence of class allocation in the ICK-based SPM is the comparison of ICK-derived probabilities in order to find the highest one during each comparison. Subpixel class labels are then predicted according to rank and number of subpixels for each class is constrained by the coarse fractions in the process. This process would be smooth if the highest probability is consistently unique during the comparisons. Sometimes, however, there is more than one highest probability value to consider. In this case, it is difficult to determine which to select.

A simple example is provided in Fig. 1; see Example I. Suppose the fraction of a class, denoted as a gray class, is 50%, and the scale factor $S = 2$. The ICK-derived conditional probabilities of the gray class in a coarse pixel are shown in Fig. 1(a). Amongst the four fine pixels, two should be allocated to the gray class. As 0.9 is the highest probability among the four subpixels, the subpixel at (1, 1) is first assigned to the gray class. The second subpixel of gray class should be selected among the remaining three subpixels by comparing the three corresponding probabilities. However, the two next highest probabilities of 0.7

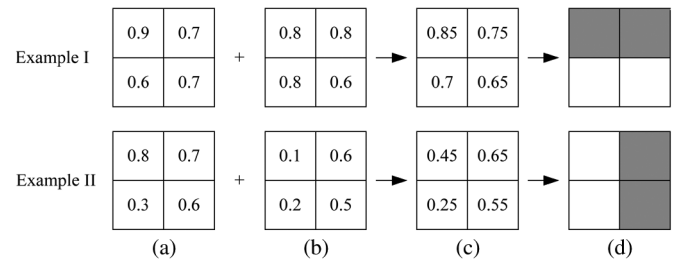


Fig. 1. ICK-derived conditional probabilities of the gray class in a coarse pixel with 2×2 fine pixels. (a) A conditional probability map. (b) Another conditional probability map obtained from additional information. (c) Integration of the two maps in (a) and (b). (d) Using (c) for class allocation given the condition that the fraction of gray class is 50%.

are at (1, 2) and (2, 2), respectively. It is impossible to determine which one should be selected as the gray class when there is only one observed coarse image.

If there is some supplemental information, however, such as another ICK-derived conditional probability map containing this coarse pixel, the second gray class subpixel may be selected out. For example, Fig. 1(b) shows the conditional probabilities of the gray class for the same four subpixels. As can be seen in Fig. 1(b), the probability of the subpixel at (1, 2) is greater than that at (2, 2), and hence the subpixel at (1, 2) should be the one assigned to the gray class. A convenient and reasonable way to integrate multiple probability maps of each class is to average these probabilities at each subpixel, and a single probability map of each class is generated in this way. Fig. 1(c) shows the integrated probabilities of the gray class for the four fine pixels that can be used for the subsequent class allocation shown in Fig. 1(d).

Errors are also unavoidable during the process of ICK-based probability estimation, and the ICK-derived probabilities from single observed coarse image may therefore not be absolutely dependable. Integration of the multiple probabilities acquired from the additional information could be an effective way to alleviate errors, and the derived integrated probability map for each class would be more accurate. Example II in Fig. 1 illustrates this problem. Again, the fraction of gray class and S are supposed to be 50% and 2. The reference gray class distribution is the same as that displayed in (d) in this example. The probability at subpixel (1, 1) from probability map (a), i.e., 0.8, is generated with some inherent error from the ICK model itself. Using only (a), because of the error at subpixel (1, 1), the subpixel will be assigned to the gray class. If, however, there exists another probability map (b) obtained from additional information where the probability at subpixel (1, 1) is 0.1, with much less error than (a). Then, by integration in (c), the error from (a) will be alleviated to a large degree, and the expected subpixel map will be generated, as in (d).

In this section, MSI are used to obtain multiple probability maps. Suppose there are R shifted images, and the subpixel shift between the r th ($r = 1, 2, \dots, R$) and the first observed coarse image is (x_r, y_r) , which means the rightward and the downward shift are x_r and y_r subpixels, respectively. If (a_m, b_m) is the coordinate of subpixel v_m in the first image, then the coordinate of its corresponding subpixel v_m^r in the r th image is $(a_m - x_r, b_m - y_r)$.

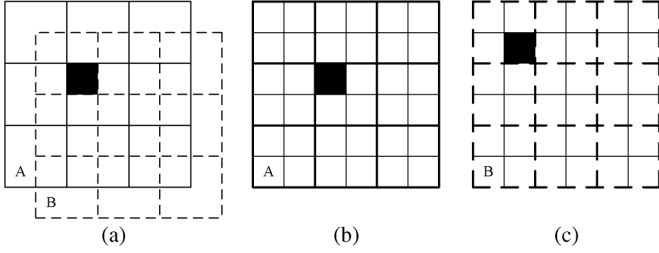


Fig. 2. (a) Two coarse images A and B with subpixel shift (1, 1). (b) and (c) The black subpixel is at (3, 3) in A and (2, 2) in B.

Fig. 2 provides an example to illustrate the relationship between the shifted images. In Fig. 2(a), there are two coarse images A (solidline) and B (dashed line) and the subpixel shift is (1, 1). Each coarse pixel in the two images is divided into 2×2 subpixels, as shown in Fig. 2(b) and (c). The black subpixel in A is at (3, 3), falling within the coarse pixel at (2, 2), while in B, it is at (2, 2), falling within the coarse pixel at (1, 1). The probability of the k th class occurrence at the black subpixel in A is related to fractions $\mathbf{a}_k^A = [a_k(V_n^A), n = 1, 2, \dots, N_A]^T$, while in B, it is related to fractions $\mathbf{a}_k^B = [a_k(V_n^B), n = 1, 2, \dots, N_B]^T$, where N_A and N_B are the number of coarse pixels in A and B, respectively. Therefore, with two images A and B, the probability of the k th class for black subpixel relies on \mathbf{a}_k^A and \mathbf{a}_k^B simultaneously. Due to the subpixel shift, $a_k(V_n^A)$ and $a_k(V_n^B)$ for the coarse pixels at the same grid n in two images are usually different from each other. The differences actually reflect the great significance of MSI.

When MSIs are used, the probability of the k th class occurrence at v_m 's corresponding subpixel v_m^r in the r th ($r = 1, 2, \dots, R$) image, denoted as $p_k(v_m^r)$, can be calculated as

$$p_k(v_m^r) = \boldsymbol{\eta}_k(v_m^r)^T \mathbf{a}_k^r + \boldsymbol{\lambda}_k(v_m^r)^T \mathbf{j}_k + \pi_k \left[1 - \text{sum} \left(\boldsymbol{\eta}_k(v_m^r)^T \right) - \text{sum} \left(\boldsymbol{\lambda}_k(v_m^r)^T \right) \right] \quad (7)$$

where $\mathbf{a}_k^r = [a_k(V_n^r), n = 1, 2, \dots, N_r]^T$ is an $(N_r \times 1)$ vector, and N_r is the number of coarse pixels in the r th image. Similarly, the ICK weights $\boldsymbol{\eta}_k(v_m^r)$ and $\boldsymbol{\lambda}_k(v_m^r)$ are computed by expression (6). The R ICK-derived probabilities of the k th class are then integrated by

$$p_k^o(v_m) = \frac{1}{R} \sum_{r=1}^R p_k(v_m^r). \quad (8)$$

An extra step is to normalize the K integrated probabilities by

$$p_k(v_m) = \frac{p_k^o(v_m)}{\sum_{k=1}^K p_k^o(v_m)} \quad (9)$$

so that $\sum_{k=1}^K p_k(v_m) = 1$. Fig. 3 displays the flowchart of the proposed ICK-based SPM with MSI.

Note that when the R ICK-derived probabilities are integrated by expression (8), the subpixel shifts (x_r, y_r) ($r = 1, 2, \dots, R$) should be estimated in advance to locate v_m 's corresponding subpixel v_m^r in the r th image. Usually, the MSIs are obtained by a sensor taking images over the same area at different times. Although these images are from

the same site, they are not completely identical, due to the slight relative translations between the satellite and Earth. In this paper, these images were assumed to be translated horizontally and vertically at subpixel level, ignoring rotation and deformation. Phase correlation is a widely used technique for image registration and is capable of measuring the relative shift between two images at subpixel level [56]. This technique was applied for MSI subpixel shift estimation.

III. EXPERIMENTS

In this section, three experiments on different types of remote sensing images were carried out to demonstrate the effectiveness and advantages of the proposed SPM method. Four SPM methods were compared: HNN-based SPM (HNNB), HNN-based SPM with MSI (HNNB_MSI), ICK-based SPM (ICKB), and ICK-based SPM with MSI (ICKB_MSI). All experiments were tested on an Intel Core i7 Processor at 3.40-GHz with the Matlab 7.1 version. For ICKB and ICKB_MSI, a set of 5×5 coarse pixel neighbors were chosen for each coarse pixel, as was done in [30]. The parameters in HNNB and HNNB_MSI were the same as those in [57]: all the weighting constants in the network energy function were set to 1, the steepness of the tanh function was set to 10, the time step was set to 0.001, and the number of iterations was set to 1000.

A. Experimental Setup

In the first two experiments, synthetic coarse images were studied in order to avoid the errors due to soft classification and co-registration and solely concentrate on the performance of the proposed SPM method. The coarse images were created by degrading the reference land cover maps via a $S \times S$ mean filter and considered as outputs of soft classification (i.e., fractions). The task of SPM methods is to generate land cover maps having the same spatial resolution as the reference maps by zooming in on the degraded images with scale factor S . Another advantage of using synthetic coarse images is that the reference land cover maps are completely reliable for the purpose of accuracy assessment. This has also been a popular approach in many existing SPM literature. In addition, the MSIs were generated by shifting the fine spatial resolution land cover maps, and the subpixels shifts were therefore known, which can avoid the errors caused by subpixel shift estimation. In each experiment, four shifted images were used, and the subpixel shifts at the scale factor S were assumed to be $(0, 0)$, $(\text{floor}(S/2), 0)$, $(0, \text{floor}(S/2))$ and $(\text{floor}(S/2), \text{floor}(S/2))$, where $\text{floor}(\bullet)$ is a function that takes the integer nearest to \bullet but not larger than it. Note that in the two experiments on synthetic coarse images, the number of subpixels for each class is strictly maintained (for all four SPM methods) according to the coarse fraction data. This is because there is no error in the synthetic coarse fraction data. The relevant class allocation method is introduced in Section II-A.

In the last experiment, real image data were used for tests: a Landsat ETM+ image and a time series of MODIS images of the same site. Four MODIS images obtained on different dates were used as MSI. Soft classification was implemented on the MODIS images, and SPM was conducted subsequent to that. The task of SPM in this experiment was to predict the distribution of land cover classes at the spatial resolution of the Landsat

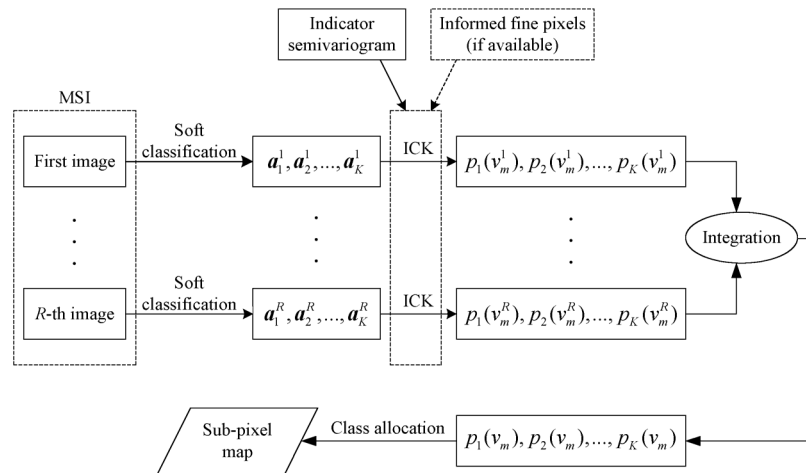


Fig. 3. Flowchart of the proposed algorithm.

ETM+ image for the coarse spatial resolution MODIS images. The hard classified map of the Landsat ETM+ image was used as a reference map for accuracy assessment.

SPM is essentially a hard classification technique, which is carried out at subpixel level. The accuracy of hard classification algorithms is usually evaluated quantitatively by the overall accuracy in terms of the percentage of correctly classified pixels (PCC). Therefore, this index was used for accuracy assessment on SPMs in the experiments. To evaluate the statistical significance in accuracy for different SPM algorithms, McNemar's test [58] was also used. The significance of difference between two classifiers is determined by

$$z = \frac{f_{01} - f_{10}}{\sqrt{f_{01} + f_{10}}} \quad (10)$$

where f_{01} are the number of pixels that are correctly classified in result 0 but incorrectly classified in result 1, and f_{10} vice versa. Using the 95% degree of confidence level, the difference between two classification results is considered to be statistically significant if $|z| > 1.96$.

B. Experiment 1: Synthetic Coarse Image of a Land Cover Map in Bath, UK

In the first experiment, a land cover map of an area in Bath, U.K., was studied. It is shown in Fig. 4 (provided by Dr. A. J. Tatem); see [59] for more details. Contained are 360×360 pixels with a pixel size of $0.6 \text{ m} \times 0.6 \text{ m}$, covering the following four classes: roads (with global fraction 8.77%), trees (with global fraction 17.07%), buildings (with global fraction 13.43%), and grass (with global fraction 60.73%). The roads and buildings have regular spatial distribution with linear features, which mainly appear as straight lines and right-angles, respectively. As for the trees, the spatial pattern is more complex and irregular. The fine spatial resolution map was degraded by a mean filter with scale 10 to produce the fraction maps of four classes shown in the first column in Fig. 5, where white indicates a fraction of 100%, and black indicates 0%. That is, each coarse pixel has a size of $6 \text{ m} \times 6 \text{ m}$, and each fraction map contains 36×36 pixels. These fraction maps were then used as input of SPM.

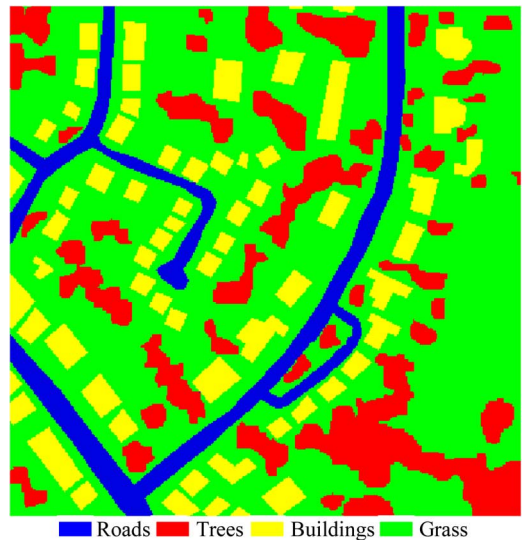


Fig. 4. Reference land cover map in experiment 1.

Using the fractions in the first column in Fig. 5 and the indicator semivariogram extracted from the fine spatial resolution land cover map in Fig. 4, the ICK-derived conditional probability map with 360×360 pixels of each class was generated, as shown in the second column in Fig. 5. The third column in Fig. 5 presents the ICK-derived probability maps produced by the proposed ICKB_MSI model. From visual comparison, we can conclude that the probability maps generated by ICKB_MSI provide more detailed information and the boundaries of land cover objects are clearer. This phenomenon indicates that ICKB_MSI can produce more accurate probabilities than ICKB. After computing the probabilities, class allocation was then implemented to generate hard classified subpixel maps by comparing these probabilities.

Fig. 6(b) and (d) shows the SPM results of the ICKB and ICKB_MSI. To fully demonstrate the advantages of the proposed method, SPM results of the HNNB and HNNB_MSI are also exhibited in Fig. 6(a) and (c). From the visual comparison of the four subpixel maps, we can see clearly that with MSI, both HNN and ICK models are capable of producing more satisfying

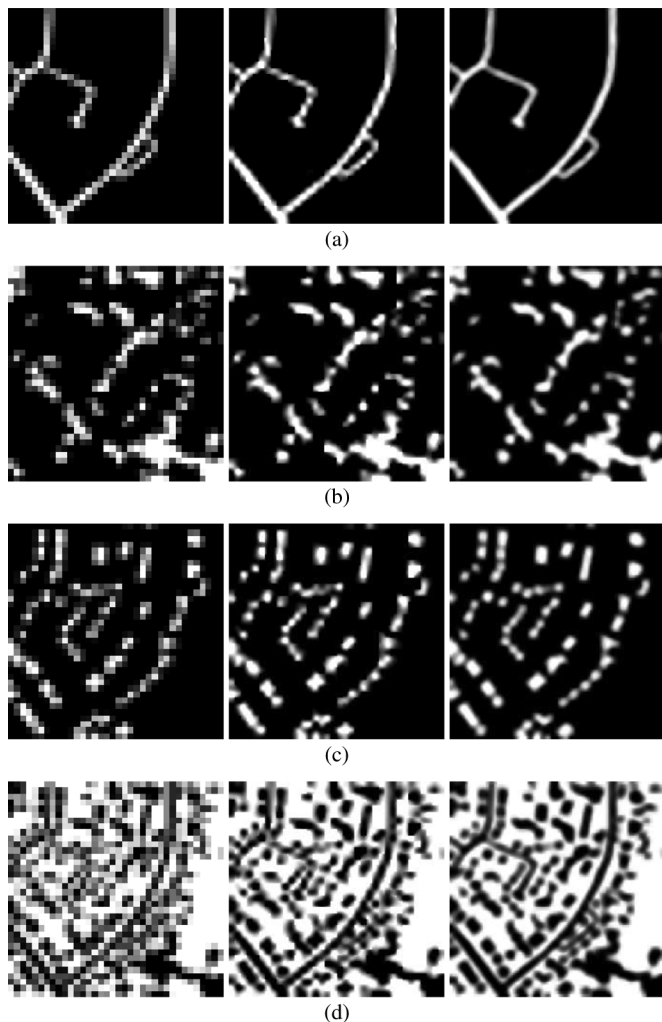


Fig. 5. From left to right: Fraction maps, ICK-derived probability maps from ICKB and ICK-derived probability maps from ICKB_MSI. (a) Roads. (b) Trees. (c) Buildings. (d) Grass.

SPM results than does the single observed coarse image. Specifically, many linear artifacts are yielded by conventional HNNB and ICKB. The result yielded by ICKB, also, looks smoother and more continuous than that by HNNB, and there are fewer linear artifacts in the ICKB result. This is because prior spatial structure information is incorporated into ICKB to alleviate the uncertainty in SPM, and thus the result will be much closer to the reference land cover map, as mentioned above in the introduction. In the HNNB_MSI result, some speckle artifacts appear, and the boundary between each class is relatively rough. Inheriting the advantage of using prior spatial structure information in ICKB, in the ICKB_MSI result, most of the land objects are recovered effectively, and the improvement is considerably pronounced when MSIs are used. Among the four SPM methods, ICKB_MSI produces the most satisfying subpixel map.

Table I displays the PCC of each SPM method. In a coarse image, there are always some pure pixels containing only one land cover class. SPM assigns all subpixels within the pure pixel to the same class to which the pure pixel belongs. This simple copy process raises accuracy without providing any useful information about the SPM algorithms' performances [15]. To eliminate the influence brought by the pure pixels, we also evalu-

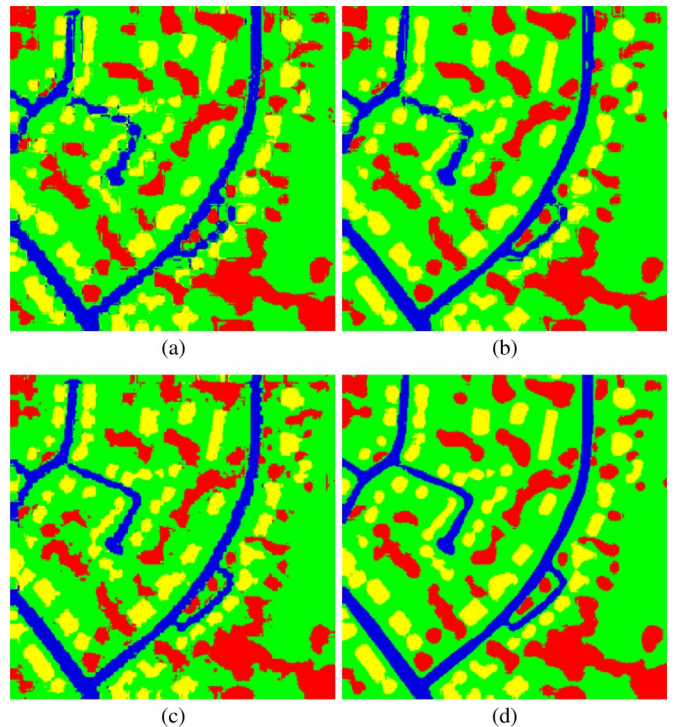


Fig. 6. SPM results in experiment 1 produced by (a) HNNB, (b) ICKB, (c) HNNB_MSI, and (d) ICKB_MSI.

TABLE I
PCC (%) OF THE FOUR SPM METHODS IN EXPERIMENT 1

	HNNB	ICKB	HNNB_MSI	ICKB_MSI
Including pure pixels	89.69	92.45	92.11	95.54
Excluding pure pixels	85.43	89.33	88.84	93.70

ated the accuracy when pure pixels are excluded in the statistics. Values in bold indicate the highest accuracy. Similar to the visual comparison, more accurate SPM results can be obtained with MSI. The ICK model outperforms the HNN model, no matter whether MSIs are applied in HNN in this experiment. Using MSI, the ICK model is able to generate the most accurate SPM result among the four methods. More precisely, the accuracy for each class of ICKB_MSI is the highest, and the PCC of it is 5.85%, 3.09%, and 3.43% greater than those of HNNB, ICKB, and HNNB_MSI when considering all pixels for accuracy statistics. Excluding pure pixels, the differences in accuracy between the four methods are more distinct: the PCC of ICKB_MSI is 8.27%, 4.37%, and 4.86% greater than that of HNNB, ICKB, and HNNB_MSI, respectively. The advantages of the proposed ICKB_MSI can also be confirmed by the McNemar's test results in Table II. One can see from Table II that using MSIs, both HNNB_MSI and ICKB_MSI have significantly higher PCC than does the single observed coarse image. Moreover, ICKB_MSI achieves significantly higher accuracy than other three SPM methods.

In addition, Fig. 7 presents the PCC of the four SPM methods with $S = 5, 10, 15,$ and 20 when excluding pure pixels for accuracy statistics. It can be concluded from the bar chart that as

TABLE II
MCNEMAR'S TEST FOR SPM METHODS IN EXPERIMENT 1

	ICKB vs	HNNB_MSI vs	ICKB_MSI vs
HNNB	42.1081	25.3082	71.0868
ICKB		-3.9533	48.7943
HNNB_MSI			46.3061
ICKB_MSI			

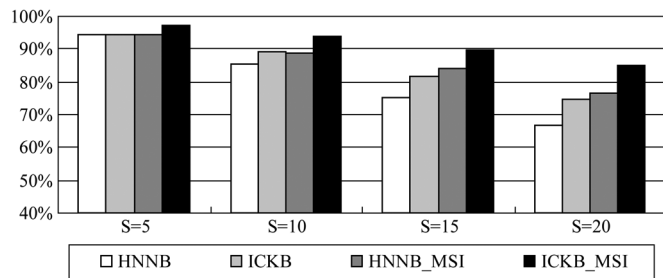


Fig. 7. PCC (excluding pure pixels) of the four SPM methods at four scales: 5, 10, 15, and 20.

the scale increases, the accuracy of all four methods decreases. The reason for this phenomenon is that the SPM process becomes more complicated with higher scale factors, as for every coarse pixel, the locations of more subpixels need to be estimated and uncertainty increases. Because of the use of MSIs, the accuracy of both HNNB and ICKB increases greatly, except for scale 5 as at this scale, SPM is relatively simple, and HNNB is able to produce highly accurate result. In fact, as the scale increases, the advantage of the proposed ICKB_MSI method becomes more obvious, generating the most accurate SPM results at all four scales. At scale 20, especially, the PCC of ICKB_MSI still reaches about 85%, while the PCC of other three methods is much less than 80%. This reveals that ICKB_MSI could be a promising approach for the large scale situation.

C. Experiment 2: Synthetic Coarse Image of a Land Cover Map in Washington, DC

The second experiment is to test the proposed method for area with large number of classes and complex land cover patterns. A part of Hyperspectral Digital Imagery Collection Experiment airborne hyperspectral data from the Washington DC Mall (191 bands with 3-m spatial resolution) was used for the test [60]. The studied area has a size of 240×296 pixels with seven classes: shadow, water, road, tree, grass, roof, and trail. The reference land cover map of the studied site is shown in Fig. 8, which was obtained with the tensor discriminative locality alignment-based classification of the hyperspectral data in [61]. The synthetic coarse image was generated by degrading the reference land cover map with $S = 8$, as shown in the first column in Fig. 9. The second and third columns of Fig. 9 show the ICK-derived conditional probability maps of seven classes with ICKB and ICKB_MSI, respectively. The indicator semivariogram used in ICK model was extracted from Fig. 8.

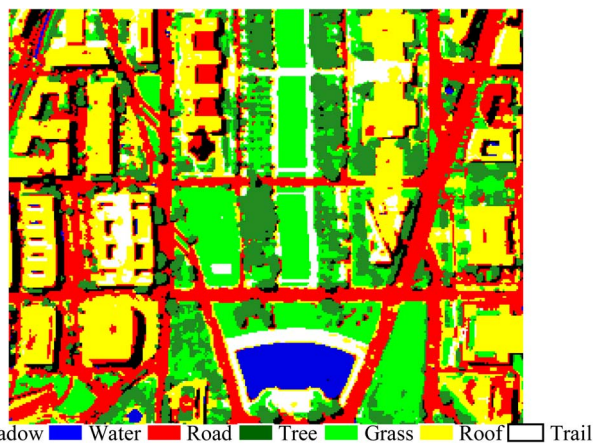


Fig. 8. Reference land cover map in experiment 2.

It can be observed that the seven probability maps derived by ICKB_MSI provide visually clearer information of land cover.

Fig. 10(a)–(d) shows the SPM results of HNNB, ICKB, HNNB_MSI, and ICKB_MSI. As can be concluded from visual comparison of the four maps, the proposed ICKB_MSI generated the best result. For example, the continuity of the trail class in the center of Fig. 10(d) is the strongest and is the closest to that in the reference map in Fig. 8; the reconstruction of the boundaries of water and road class in Fig. 10(d) is more satisfying in comparison with Fig. 10(a)–(c). Table III gives the PCC of the four SPM methods. Similar to the conclusion of visual comparison, ICKB_MSI achieves the highest accuracy among the four methods. The McNemar's test results in Table IV indicate that the PCC of ICKB_MSI is significantly higher than that of HNNB, ICKB, and HNNB_MSI.

D. Experiment 3: Real Data

To further validate the advantages of the proposed SPM method, tests on real data were implemented in the third experiment. Two sets of image data were used, including a time series of MODIS images and a Landsat ETM+ image. They cover an area located in Quebec province, Canada, mainly made up of lakes and land. Four MODIS 250-m spatial resolution images on four close days in 2002 were acquired: 21 June, 30 June, 5 July, and 6 August. The Landsat ETM+ image with a spatial resolution of 30 m obtained on 10 July 2002 was used to provide ground truth data. Only the images acquired in the near infrared band of the two sets of data were used because the land cover classes were highly separable in this band. The MODIS image obtained on 5 July was used as a reference image for subpixel shift estimation of MSI. Further details on the description of site and data can be found in [62]. The subpixel shifts of the images measured by a phased correlation technique are (5, 6), (4, 7) and (1, 5) subpixels (i.e., (156 m, 188 m), (125 m, 219 m), and (31 m, 156 m)) for images acquired on 21 June, 30 June, and 6 August.

The original Landsat ETM+ image has a size of 865×927 pixels. Using nearest neighbor interpolation, it was interpolated to 872×936 pixels, 8×8 times of the size of MODIS images (109×117 pixels). The pixels in the Landsat ETM+ image were supposed to be pure materials, and an unsupervised k -means

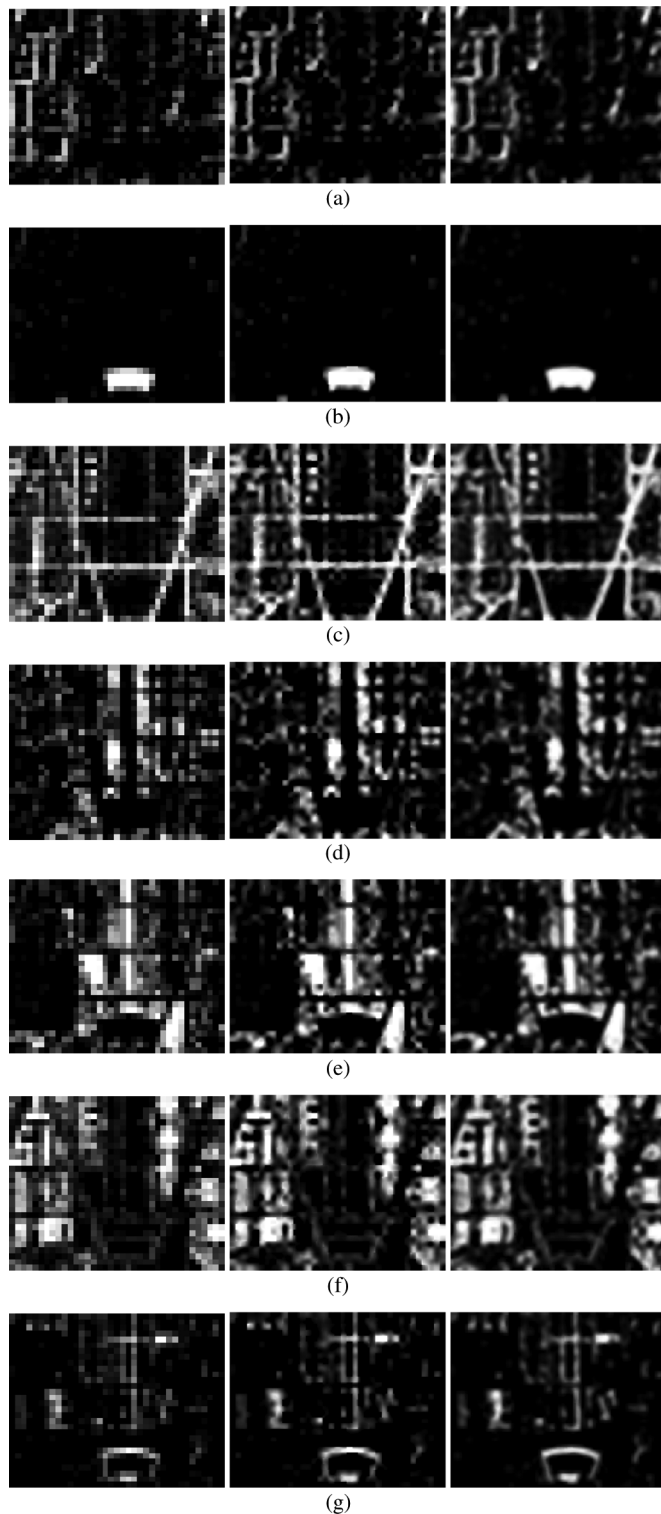


Fig. 9. From left to right: Fraction maps, ICK-derived probability maps from ICKB and ICK-derived probability maps from ICKB_MSI. (a) Shadow. (b) Water. (c) Road. (d) Tree. (e) Grass. (f) Roof. (g) Trail.

classifier [63] was employed to generate the hard classified ground truth map from this image. Without ground survey, it is difficult to conduct a rigorous evaluation of the accuracy of reference data. Through visual interpretation, however, the generated reference map looks highly similar to the Landsat ETM+ image [see Fig. 11(a) and (b)]. A sub-site was selected

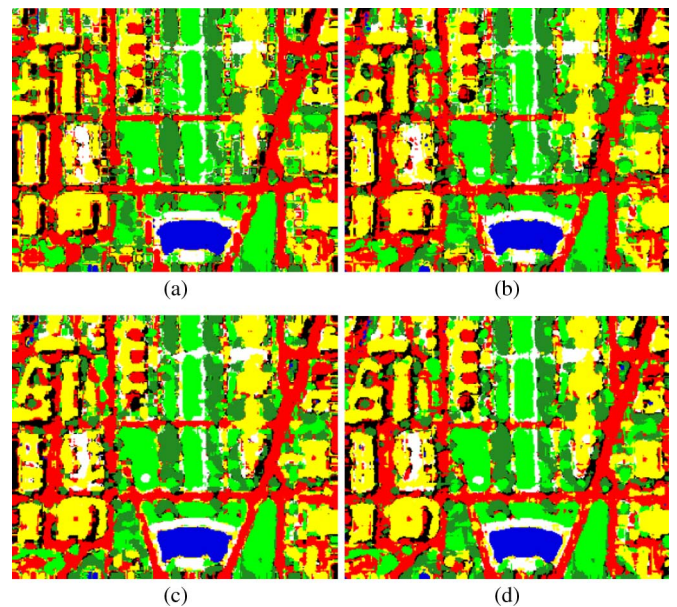


Fig. 10. SPM results in experiment 2 produced by (a) HNNB, (b) ICKB, (c) HNNB_MSI, and (d) ICKB_MSI.

TABLE III
PCC (%) OF THE FOUR SPM METHODS IN EXPERIMENT 2

	HNNB	ICKB	HNNB_MSI	ICKB_MSI
Including pure pixels	64.98	66.64	70.92	72.54
Excluding pure pixels	61.85	63.66	68.32	70.08

TABLE IV
MCNEMAR'S TEST FOR SPM METHODS IN EXPERIMENT 2

	ICKB vs	HNNB_MSI vs	ICKB_MSI vs
HNNB	10.7968	33.3190	44.0003
ICKB		24.2095	40.1149
HNNB_MSI			10.7551
ICKB_MSI			

for test, labeled as sub-site A in Fig. 11(b). It has a size of 320×320 pixels. The classified map at sub-site B was used as prior spatial structure information and the indicator semivariogram was extracted from it for ICKB and ICKB_MSI. This process was based on the assumption that the distribution of classes at sub-site B was available, and the spatial pattern of this area was similar to sub-site A.

The MODIS images were soft classified by an unsupervised fuzzy c -means algorithm [4] ($c = 2$). The weighting parameter that determines the degree of fuzziness was set to 2. After that, four SPM methods were carried out on the fraction images, with a zoom factor $S = 8$. When the estimated fractions were used to strictly maintain the subpixels of each class during the class allocation process, a large number of isolated pixels were produced in the SPM results. In this way, the generated subpixel maps appeared to be dominated by a speckled

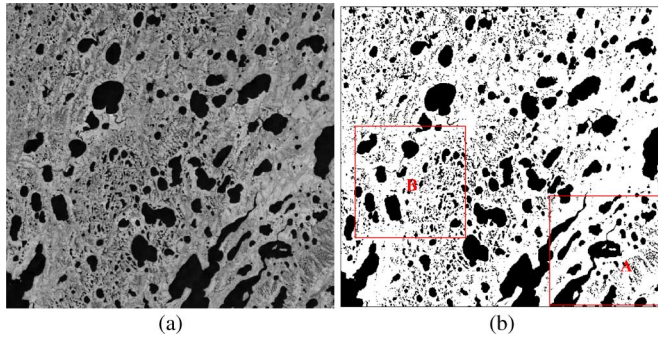


Fig. 11. The Landsat ETM+ image. (a) Near-infrared band image. (b) Hard classified map, where white and black pixels denote land and water, respectively.

pattern, which greatly suppressed the performances of the SPM methods. This phenomenon was caused by the errors in the soft classification. For example, suppose in the coarse image there is a pure pixel covering the class, water. By SPM, all 8×8 subpixels within this pixel should be allocated to water. However, if the estimated fraction of water for this pixel is 12.5%, by class allocation, eight subpixels should be allocated to water. In this case, these eight subpixels are produced by errors from soft classification and are quite likely to appear as noise in the SPM result. For sub-site A, the PCC values (considering all pixels) of four SPM methods are between 80% and 81% when coarse fractions were strictly maintained. To alleviate the influence of such errors from soft classification, in this experiment, the fractions were used in probability estimation but not in the pivotal class allocation process. Instead, a simple class allocation method was applied whereby each subpixel was allocated to the class with the highest probability. The SPM results for the two sub-sites are shown in Fig. 12.

As can be seen from the results in Fig. 12, there are some jagged boundaries in the HNNB and ICKB results, appearing as right-angle shape, as shown in Fig. 12(a) and (b). This phenomenon conflicts with the class distribution in the ground reference maps [Fig. 11(b)]. With MSIs, the performances of both HNNB and ICKB were enhanced. The boundaries in Fig. 12(c) and (d) looks smoother and more places were correctly classified, such as those places with small lakes. While focusing on Fig. 12(c), it is found that in the HNNB_MSI result, some block objects classified as land lie within some large lakes. In the ground truth maps, however, these large lakes are of hole-shape, as shown in Fig. 11(b). Therefore, places covered by these block objects in Fig. 12(c) were misclassified. This is not the case, however, in ICKB_MSI result. Among the four methods, the proposed method generated the SPM result that is the closest to the reference maps.

Table V lists the PCC of the four SPM approaches. Note that PCC in this experiment was calculated taking account of all pixels in SPM results. The pure pixels in coarse images were not excluded as whether a pixel is pure or not is determined by the soft classifier (fuzzy c -means algorithm in this experiment). We are also concerned about the performance of soft classifier when real coarse images are studied for SPM. This is different from the previous two experiments, where synthetic coarse images were studied and no soft classifier was applied and hence no error exists in soft classification in fact. The PCC

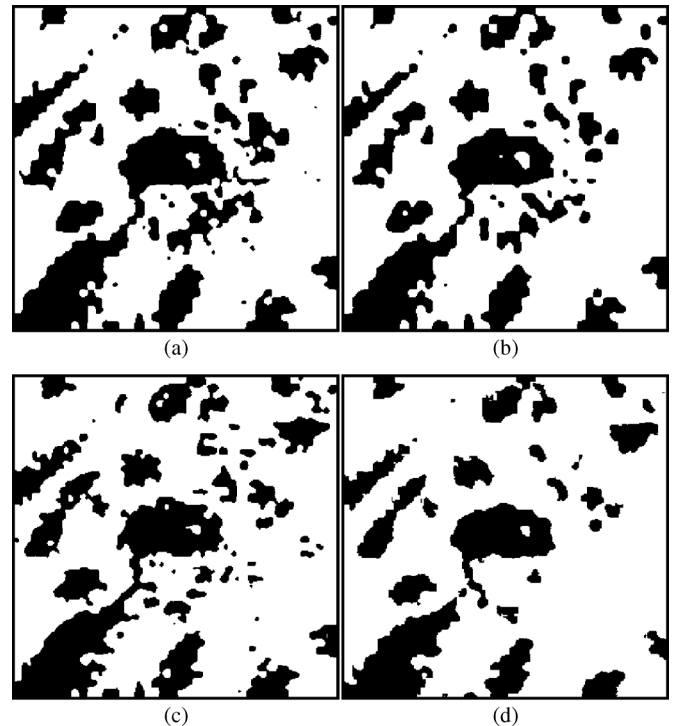


Fig. 12. SPM results of the real MODIS data produced by (a) HNNB, (b) ICKB, (c) HNNB_MSI, and (d) ICKB_MSI. White and black pixels denote land and water, respectively.

TABLE V
PCC (%) OF THE FOUR SPM METHODS IN EXPERIMENT 3

HNNB	ICKB	HNNB_MSI	ICKB_MSI
82.18	82.98	83.20	84.15

TABLE VI
MCNEMAR'S TEST FOR SPM METHODS IN EXPERIMENT 3

	ICKB vs	HNNB_MSI vs	ICKB_MSI vs
HNNB	14.0072	10.3767	17.0608
ICKB		2.2357	10.6082
HNNB_MSI			9.5271
ICKB_MSI			

of the proposed method is 84.15%, about 2%, 1.2%, and 1% greater than that of HNNB, ICKB, and HNNB_MSI. In all, the proposed method produced the highest SPM accuracy. The McNemar's test results are shown in Table VI. It can be observed that ICKB obtains significantly higher accuracy than HNNB because ICKB makes use of prior spatial structure information. Similar to the conclusions drawn from the previous two experiments on synthetic coarse images, HNNB_MSI obtains significantly higher accuracy than HNNB, while ICKB_MSI obtains significantly higher accuracy than ICKB; the accuracy of the proposed ICKB_MSI is significantly higher than other three SPM methods.

IV. DISCUSSIONS

From the results in three experiments, we can obtain a general rank of the four SPM methods in terms of SPM accuracy: HNNB, ICKB, HNNB_MSI, and ICKB_MSI. From HNNB to ICKB_MSI, the overall performances become better in this study. The reason for the advantages of ICK-based SPM methods (i.e., ICKB and ICKB_MSI) over HNN-based methods (i.e., HNNB and HNNB_MSI) is that the former utilize prior spatial structure information while the latter are based on spatial dependence and thus fail to deal with complex spatial patterns, as mentioned in the introduction. With the aid of MSI, however, HNN is able to produce better SPM results than does ICKB. This reveals the great potentiality of MSI in SPM.

The computational efficiency is also an important factor to evaluate the four SPM methods. In each experiment, HNNB and HNNB_MSI took several hours for 1000 iterations. However, both ICKB and ICKB_MSI took less than 2 minutes. The considerably low computational burden in ICKB and ICKB_MSI is mainly due to the fact no iterations are involved in them. Therefore, the proposed method will be promising for a real-time system.

The proposed algorithm is different from the HNN-based SPM with MSI, except that the proposed algorithm is learning-based while the HNN model is based on spatial dependence assumption. For HNN-based SPM with MSI, each fine pixel also falls within multiple coarse pixels in MSI, and the fractions of classes within the corresponding multiple coarse pixels are added into the constraint term of the HNN's energy function, to provide multiple fraction constraints. Essentially, the HNN used for SPM is an optimization tool. In this model, the attribute value of each class for each subpixel (between zero and one) is changed after each iteration, and the energy function is minimized iteratively to approach a solution. With multiple fraction constraints from MSIs, therefore, a large number of iterations (usually over 1000) for the conventional HNN model are still required to generate attribute values. However, this is not the case in the proposed algorithm based on the ICK model. In the ICK-based SPM, for each subpixel v_m , fractions (those from all coarse pixels in the neighborhood window, not only the one, v_m falls within) are used in linear combination, see (5), and their weights are calculated by solving the equations in (6). No iterations are involved in the whole process. With MSIs, for each subpixel v_m , fractions in the shifted images are used and a set of ICK-derived probabilities are also calculated in the same way and without iterations. Besides, from expression (6), we can also see that no parameters are involved, and the information from informed fine pixels can also be readily coded into the new model. Consequently, the proposed algorithm inherits all the advantages of the ICK-based SPM.

As can be found from Table I and Table III, the PCC of the proposed algorithm decreases from around 94% in Table I to 70% in Table III. This is because the number of classes increases from four in experiment 1 to seven in experiment 2. Furthermore, the complexity of land cover pattern is also different in the two experiments. In Fig. 4, the roads and buildings have regular spatial distribution with linear features, which can be well recreated by the proposed SPM method. In Fig. 8, however, there are

many linear and elongated features, which are more difficult to be restored in comparison with the features in Fig. 4. We can conclude that the performance of the proposed SPM algorithm is influenced by the number of classes and spatial complexity of land cover pattern in the studied area.

Focusing on Fig. 7, it is concluded that the performance of the proposed SPM algorithm deteriorates when the zoom scale factor increases. Compared with the other three SPM methods, the proposed method is relatively less sensitive to the scale factor, suggesting the new SPM method is potential for the large scale cases.

As a preprocessing step, the soft classification has a direct influence on the SPM and errors from the former can be propagated to the latter [64]. In real word cases, the uncertainty in soft classification needs further study. The selection of MSIs is also a critical issue. In different periods, the land cover from the same area may be different due to the human activities (e.g., buildings construction) and natural changes (e.g., changes of rainfall and vegetation in different seasons) and so on. In addition, illumination and angular effects sometimes plays an important role in MSI. It makes a huge difference to an image whether it is acquired in the morning or afternoon or if the viewing angle is from the right, left, or nadir. The uncertainty in MSI data certainly has an impact on the proposed method that uses MSI as additional information. It necessitates the consideration of acquired time, illumination and angular while selecting MSI for the proposed SPM method.

V. CONCLUSION

An SPM algorithm based on ICK with MSI is proposed in this paper. The proposed algorithm utilizes MSI to provide additional constraints for the ICK-based SPM model to increase the accuracy. In detail, with extracted prior structure information, the MSI are used to obtain multiple ICK-derived conditional probability maps for each class. Then, according to the subpixels shifts of MSI, the multiple probabilities are integrated. The integrated probabilities are then used for class allocation to yield subpixel maps meeting a target spatial resolution. This new method inherits all the advantages of the ICK-based SPM model, which is capable of making use of prior spatial structure information and incorporating the information from the informed fine pixels. In addition, few parameters and iterations are involved in the new model.

Experiments based on two synthetic coarse images and a set of real MODIS images demonstrated the effectiveness and advantages of the proposed algorithm. From both visual and quantitative assessments, the conclusion can be drawn that the proposed ICK with MSI can produce more satisfying and accurate subpixel maps than conventional ICK as well as HNN-based SPM, whether or not MSI are applied in HNN.

In this study, MSI were used as the additional information for ICK-based SPM. Additional information from other source images might also be applied, under the condition that these images can provide multiple fractions at the same coarse or intermediate spatial resolution. Moreover, the additional information from different source images is expected to be integrated in the ICK-based SPM model in the future. Further work will focus on these issues.

ACKNOWLEDGMENT

The authors would like to thank Dr. A. J. Tatem of the University of Florida for providing the land cover map in the first experiment, Dr. L. Zhang of the Wuhan University for providing the land cover map in the second experiment, and Dr. A. M. Muad of the Universiti Kebangsaan Malaysia for providing the MODIS and Landsat ETM+ data used in this paper. The authors would also like to thank Dr. A. M. Muad for his helpful discussion. The valuable comments of the anonymous reviewers have greatly improved this paper.

REFERENCES

- [1] P. Fisher, "The pixel: A snare and a delusion," *Int. J. Remote Sens.*, vol. 18, no. 3, pp. 679–685, 1997.
- [2] G. M. Foody, "Sub-pixel methods in remote sensing," in *Remote Sensing Image Analysis: Including the Spatial Domain*, S. M. de Jong and F. D. van der Meer, Eds. Dordrecht, The Netherlands: Kluwer, 2006, pp. 37–49.
- [3] D. C. Heinz and C.-I. Chang, "Fully constrained least squares linear spectral mixture analysis method for material quantification in hyperspectral imagery," *IEEE Trans. Geosci. Remote Sens.*, vol. 39, no. 3, pp. 529–545, 2001.
- [4] L. Bastin, "Comparison of fuzzy c-means classification, linear mixture modeling and MLC probabilities as tools for unmixing coarse pixels," *Int. J. Remote Sens.*, vol. 18, pp. 3629–3648, 1997.
- [5] G. M. Carpenter, S. Gopal, S. Macomber, S. Martens, and C. E. Woodcock, "A neural network method for mixture estimation for vegetation mapping," *Remote Sens. Environ.*, vol. 70, pp. 138–152, 1999.
- [6] R. A. Schowengerdt, "On the estimation of spatial-spectral mixing with classifier likelihood functions," *Pattern Recognit. Lett.*, vol. 17, no. 13, pp. 1379–1387, 1996.
- [7] M. Brown, H. Lewis, and S. Gunn, "Linear spectral mixture models and Support Vector Machine for remote sensing," *IEEE Trans. Geosci. Remote Sens.*, vol. 38, no. 5, pp. 2346–2360, 2000.
- [8] L. Wang and X. Jia, "Integration of soft and hard classification using extended support vector machine," *IEEE Geosci. Remote Sens. Lett.*, vol. 6, no. 3, pp. 543–547, 2009.
- [9] A. Halimi, Y. Altmann, N. Dobigeon, and J. Y. Tourneret, "Nonlinear unmixing of hyperspectral images using a generalized bilinear model," *IEEE Trans. Geosci. Remote Sens.*, vol. 49, no. 11, pp. 4153–4162, 2011.
- [10] P. M. Atkinson, "Mapping subpixel boundaries from remotely sensed images," *Innov. GIS*, vol. 4, pp. 166–180, 1997.
- [11] J. Verhoeve and R. DeWulf, "Land-cover mapping at subpixel scales using linear optimization techniques," *Remote Sens. Environ.*, vol. 79, no. 1, pp. 96–104, 2002.
- [12] A. J. Tatem, H. G. Lewis, P. M. Atkinson, and M. S. Nixon, "Super-resolution target identification from remotely sensed images using a Hopfield neural network," *IEEE Trans. Geosci. Remote Sens.*, vol. 39, no. 4, pp. 781–796, 2001.
- [13] A. J. Tatem, H. G. Lewis, P. M. Atkinson, and M. S. Nixon, "Multi-class land cover mapping at the subpixel scale using a Hopfield neural network," *Int. J. Appl. Earth Observ. Geoinf.*, vol. 3, no. 2, pp. 184–190, 2001.
- [14] A. M. Muad and G. M. Foody, "Impact of land cover patch size on the accuracy of patch area representation in HNN-based super resolution mapping," *IEEE J. Sel. Topics Appl. Earth Observ. Remote Sens.*, vol. 5, no. 5, pp. 1418–1427, 2012.
- [15] K. C. Mertens, L. P. C. Verbeke, E. I. Ducheyne, and R. DeWulf, "Using genetic algorithms in subpixel mapping," *Int. J. Remote Sens.*, vol. 24, no. 21, pp. 4241–4247, 2003.
- [16] P. M. Atkinson, "Sub-pixel target mapping from soft-classified, remotely sensed imagery," *Photogramm. Eng. Remote Sens.*, vol. 71, no. 7, pp. 839–846, 2005.
- [17] K. C. Mertens, B. D. Basets, L. P. C. Verbeke, and R. DeWulf, "A subpixel mapping algorithm based on subpixel/pixel spatial attraction models," *Int. J. Remote Sens.*, vol. 27, no. 15, pp. 3293–3310, 2006.
- [18] Y. Ge, S. Li, and V. C. Lakhan, "Development and testing of a subpixel mapping algorithm," *IEEE Trans. Geosci. Remote Sens.*, vol. 47, no. 7, pp. 2155–2164, 2009.
- [19] Q. Wang, L. Wang, and D. Liu, "Particle swarm optimization-based subpixel mapping for remote-sensing imagery," *Int. J. Remote Sens.*, vol. 33, no. 20, pp. 6480–6496, 2012.
- [20] Q. Wang, L. Wang, and D. Liu, "Integration of spatial attractions between and within pixels for subpixel mapping," *J. Syst. Eng. Electron.*, vol. 23, no. 2, pp. 293–303, 2012.
- [21] T. Kasetkasem, M. K. Arora, and P. K. Varshney, "Super-resolution land-cover mapping using a Markov random fieldbased approach," *Remote Sens. Environ.*, vol. 96, no. 3/4, pp. 302–314, 2005.
- [22] V. A. Tolpekin and A. Stein, "Quantification of the effects of land-cover-class spectral separability on the accuracy of Markov-random-field based superresolution mapping," *IEEE Trans. Geosci. Remote Sens.*, vol. 47, no. 9, pp. 3283–3297, 2009.
- [23] P. M. Atkinson, "Issues of uncertainty in super-resolution mapping and their implications for the design of an inter-comparison study," *Int. J. Remote Sens.*, vol. 30, no. 20, pp. 5293–5308, 2009.
- [24] K. C. Mertens, L. P. C. Verbeke, and R. DeWulf, "Sub-pixel mapping with neural networks: Real-world spatial configurations learned from artificial shapes," in *Proc. 4th Int. Symp. Remote Sens. Urban Areas*, Regensburg, Germany, 2003, pp. 117–121.
- [25] L. Wang, Y. Zhang, and J. Li, "BP neural network based subpixel mapping method," in *Proc. Int. Conf. Intell. Comput.*, 2006, pp. 755–760.
- [26] L. Zhang, K. Wu, Y. Zhong, and P. Li, "A new subpixel mapping algorithm based on a BP neural network with an observation model," *Neurocomput.*, vol. 71, no. 10–12, pp. 2046–2054, 2008.
- [27] D. Nigusie, R. Zurita-Milla, and J. G. P. W. Clevers, "Possibilities and limitations of artificial neural networks for subpixel mapping of land cover," *Int. J. Remote Sens.*, vol. 32, no. 22, pp. 7203–7226, 2011.
- [28] K. C. Mertens, L. P. C. Verbeke, T. Westra, and R. De Wulf, "Sub-pixel mapping and subpixel sharpening using neural network predicted wavelet coefficients," *Remote Sens. Environ.*, vol. 91, pp. 225–236, 2004.
- [29] P. M. Atkinson, "Super-resolution land cover classification using the two-point histogram," in *Proc. Geostatist. Environ. Appl. (GeoENV IV)*, 2004, pp. 15–28.
- [30] A. Boucher and P. C. Kyriakidis, "Super-resolution land cover mapping with indicator geostatistics," *Remote Sens. Environ.*, vol. 104, no. 3, pp. 264–282, 2006.
- [31] A. Boucher and P. C. Kyriakidis, "Integrating fine scale information in super-resolution land-cover mapping," *Photogramm. Eng. Remote Sens.*, vol. 73, no. 8, pp. 913–921, 2008.
- [32] A. Boucher, P. C. Kyriakidis, and C. Cronkite-Ratcliff, "Geostatistical solutions for super-resolution land cover mapping," *IEEE Trans. Geosci. Remote Sens.*, vol. 46, no. 1, pp. 272–283, 2008.
- [33] A. Boucher, "Sub-pixel mapping of coarse satellite remote sensing images with stochastic simulations from training images," *Math. Geosci.*, vol. 41, pp. 265–290, 2009.
- [34] H. Jin, G. Mountrakis, and P. Li, "A super-resolution mapping method using local indicator variograms," *Int. J. Remote Sens.*, vol. 33, no. 24, pp. 7747–7773, 2012.
- [35] Y. Makido and A. Shortridge, "Weighting function alternatives for a subpixel allocation model," *Photogramm. Eng. Remote Sens.*, vol. 73, no. 11, pp. 1233–1240, 2007.
- [36] Y. Makido, "Land-cover mapping at subpixel scales," Ph.D. dissertation, Michigan State Univ., East Lansing, MI, USA, 2006.
- [37] M. Collins and M. De Jong, "Neutralizing target superresolution algorithms," *IEEE Geosci. Remote Sens. Lett.*, vol. 1, no. 4, pp. 318–321, 2004.
- [38] G. M. Foody, "Sharpening fuzzy classification output to refine the representation of subpixel land cover distribution," *Int. J. Remote Sens.*, vol. 19, no. 13, pp. 2593–2599, 1998.
- [39] P. Aplin and P. M. Atkinson, "Sub-pixel land cover mapping for per-field classification," *Int. J. Remote Sens.*, vol. 22, no. 14, pp. 2853–2858, 2001.
- [40] P. M. Atkinson, "Super-resolution mapping using the two-point histogram and multi-source imagery," in *Proc. Geostatist. Environ. Appl. (GeoENV VI)*, 2008, pp. 307–321.
- [41] M. Q. Nguyen, P. M. Atkinson, and H. G. Lewis, "Superresolution mapping using a Hopfield neural network with LIDAR data," *IEEE Geosci. Remote Sens. Lett.*, vol. 2, no. 3, pp. 366–370, 2005.

- [42] F. Ling, F. Xiao, Y. Du, H. Xue, and X. Ren, "Waterline mapping at the subpixel scale from remote sensing imagery with high-resolution digital elevation models," *Int. J. Remote Sens.*, vol. 29, no. 6, pp. 1809–1815, 2008.
- [43] F. Ling, X. Li, F. Xiao, S. Fang, and Y. Du, "Object-based subpixel mapping of buildings incorporating the prior shape information from remotely sensed imagery," *Int. J. Appl. Earth Observ. Geoinf.*, vol. 18, pp. 283–292, 2012.
- [44] M. Q. Nguyen, P. M. Atkinson, and H. G. Lewis, "Super-resolution mapping using Hopfield neural network with panchromatic imagery," *Int. J. Remote Sens.*, vol. 32, no. 21, pp. 6149–6176, 2011.
- [45] M. Q. Nguyen, P. M. Atkinson, and H. G. Lewis, "Superresolution mapping using a Hopfield neural network with fused images," *IEEE Trans. Geosci. Remote Sens.*, vol. 44, no. 3, pp. 736–749, 2006.
- [46] F. Ling, Y. Du, F. Xiao, H. Xue, and S. Wu, "Super-resolution land-cover mapping using multiple subpixel shifted remotely sensed images," *Int. J. Remote Sens.*, vol. 31, no. 19, pp. 5023–5040, 2010.
- [47] A. M. Muad and G. M. Foody, "Super-resolution analysis for accurate mapping of land cover and land cover pattern," in *Proc. Int. Geosci. Remote Sens. Symp.*, 2010, pp. 502–505.
- [48] P. M. Atkinson, "Downscaling in remote sensing," *Int. J. Appl. Earth Observ. Geoinf.*, vol. 22, pp. 106–114, 2013.
- [49] Y. Lu and M. Inamura, "Spatial resolution improvement of remote sensing images by fusion of subpixel-shifted multi-observation images," *Int. J. Remote Sens.*, vol. 24, no. 23, pp. 4647–4660, 2003.
- [50] A. M. Muad and G. M. Foody, "Super-resolution mapping of lakes from imagery with a coarse spatial and fine temporal resolution," *Int. J. Appl. Earth Observ. Geoinf.*, vol. 15, pp. 79–91, 2012.
- [51] X. Xu, Y. Zhong, L. Zhang, and H. Zhang, "Sub-pixel mapping based on a MAP model with multiple shifted hyperspectral imagery," *IEEE J. Sel. Topics Appl. Earth Observ. Remote Sens.*, vol. 6, no. 2, pp. 580–593, 2013.
- [52] S. C. Park, M. K. Park, and M. G. Kang, "Super-resolution image reconstruction: A technical overview," *IEEE Signal Process. Mag.*, vol. 20, no. 3, pp. 21–36, 2003.
- [53] Y. Shao and R. S. Lunetta, "Sub-pixel mapping of tree canopy, impervious surfaces, cropland in the Lurentian great lakes basin using MODIS time-series data," *IEEE J. Sel. Topics App. Earth Observ. Remote Sens.*, vol. 4, no. 2, pp. 336–347, 2011.
- [54] P. M. Atkinson, C. Jeganathan, J. Dash, and C. Atzberger, "Inter-comparison of four models for smoothing satellite sensor time-series data to estimate vegetation phenology," *Remote Sens. Environ.*, vol. 123, pp. 400–417, 2012.
- [55] Q. Wang, W. Shi, and L. Wang, "Allocating classes for soft-then-hard subpixel mapping algorithms in units of class," *IEEE Trans. Geosci. Remote Sens.*, submitted for publication.
- [56] G. S. Manuel, T. T. Samuel, and R. F. James, "Efficient subpixel image registration algorithms," *Opt. Lett.*, vol. 33, no. 2, pp. 156–158, 2008.
- [57] L. Wang and Q. Wang, "Subpixel mapping using Markov random field with multiple spectral constraints from subpixel shifted remote sensing images," *IEEE Geosci. Remote Sens. Lett.*, vol. 10, no. 3, pp. 598–602, 2013.
- [58] G. M. Foody, "Thematic map comparison evaluating the statistical significance of differences in classification accuracy," *Photogramm. Eng. Remote Sens.*, vol. 70, no. 5, pp. 627–633, 2004.
- [59] A. J. Tatem, "Super-resolution land cover mapping from remotely sensed imagery using a Hopfield neural network," Ph.D. dissertation, Univ. of Southampton, Southampton, U.K., 2002.
- [60] D. Landgrebe, *Signal Theory Methods in Multispectral Remote Sensing*. Hoboken, NJ, USA: Wiley, 2003.
- [61] L. Zhang, L. Zhang, D. Tao, and X. Huang, "Tensor discriminative locality alignment for hyperspectral image spectral-spatial feature extraction," *IEEE Trans. Geosci. Remote Sens.*, vol. 51, no. 1, pp. 242–256, 2013.
- [62] A. M. Muad, "Super-resolution mapping," Ph.D. dissertation, Univ. of Nottingham, Nottingham, U.K., 2011, pp. 160–163.
- [63] R. O. Duda, P. E. Hart, and D. G. Stork, *Pattern Classification and Scene Analysis*, 2nd ed. New York, NY, USA: Wiley, 2001.
- [64] A. Villa, J. Chanussot, J. A. Benediktsson, and C. Jutten, "Spectral unmixing for the classification of hyperspectral images at a finer spatial resolution," *IEEE J. Sel. Topics Signal Process.*, vol. 5, no. 3, pp. 521–533, 2011.



Qunming Wang received the B.S. and M.S. degrees from Harbin Engineering University, Harbin, China, in 2010 and 2012, respectively. He is currently working toward the Ph.D. degree in the Department of Land Surveying and Geo-Informatics, The Hong Kong Polytechnic University, Kowloon, Hong Kong.

His current research interests focus on remote sensing image analysis and pattern recognition.

Mr. Wang was the recipient of the Excellent Master Dissertation Award as well as the Excellent Graduates in Heilongjiang Province, China, in 2012. He has

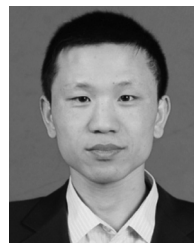
been awarded the hyper-competitive Hong Kong PhD Fellowship.



Wenzhong Shi received the Ph.D. degree from the University of Osnabrück, Vechta, Germany, in 1994.

He is currently a Professor in GIS and remote sensing, Department of Land Surveying and Geo-Informatics, The Hong Kong Polytechnic University. His current research interests include GIS and remote sensing, uncertainty and spatial data quality control, and image processing for high-resolution satellite images. He has published about 400 research articles (including over 80 SCI papers) and 10 books.

Dr. Shi received the State Natural Science Award from the State Council of China in 2007.



Ligu Wang received the Master's degree and the Ph.D. degree in signal and information processing from Harbin Institute of Technology, Harbin, China, in 2002 and 2005, respectively.

From 2006 to 2008, he held a postdoctoral research position in the Center of Information and Communications Engineering, Harbin Engineering University. He is currently a Professor in this university with research interests in remote sensing and machine learning. He has published one book titled *Processing Techniques for Hyperspectral Imagery*

(Nat. Defence Industry Press, 2013) and more than 80 papers in journals and conference proceedings.